

Solitons and Josephson-type oscillations in Bose-Einstein condensates with spin-orbit coupling and time-varying Raman frequency

F. Kh. Abdullaev,^{1,2} M. Brtko,² A. Gammal,³ and Lauro Tomio^{4,5}

¹*Physical-Technical Institute, Uzbekistan Academy of Sciences, Tashkent, Bodomzor yuli 2-b, Uzbekistan*

²*CCNH e CMCC, Universidade Federal do ABC, 09210-170 Santo André, Brazil*

³*Instituto de Física, Universidade de São Paulo, 05508-090 São Paulo, Brazil*

⁴*Instituto Tecnológico de Aeronáutica, CTA, 12228-900 São José dos Campos, Brazil*

⁵*Instituto de Física Teórica, Universidade Estadual Paulista, 01140-070 São Paulo, Brazil*



(Received 19 February 2018; published 17 May 2018)

The existence and dynamics of solitons in quasi-one-dimensional Bose-Einstein condensates with spin-orbit coupling (SOC) and attractive two-body interactions are described for two coupled atomic pseudospin components with slowly and rapidly varying time-dependent Raman frequency. By varying the Raman frequency linearly in time, it was shown that ordinary nonlinear Schrödinger-type bright solitons can be converted to striped bright solitons, and vice versa. The internal Josephson oscillations between atom number of the coupled soliton components and the corresponding center-of-mass motion are studied for different parameter configurations. In this case, a mechanism to control the soliton parameters is proposed by considering parametric resonances, which can emerge when using time-varying Raman frequencies. Full-numerical simulations confirm variational analysis predictions when applied to the region where regular solitons are expected. In the limit of high frequencies, the system is described by a time-averaged Gross-Pitaevskii formalism with renormalized nonlinear and SOC parameters and modified phase-dependent nonlinearities. By comparing full-numerical simulations with averaged results, we have also studied the lower limits for the frequency of Raman oscillations in order to obtain stable soliton solutions.

DOI: [10.1103/PhysRevA.97.053611](https://doi.org/10.1103/PhysRevA.97.053611)

I. INTRODUCTION

A progressively growing interest in the physics of Bose-Einstein condensates (BECs) with spin-orbit coupling (SOC) has been observed in recent years [1–5]. For the coupling, different forms of Rashba [6] and Dresselhaus [7], as well as a mixture of them, have been realized [8]. Important forms for the nonlinear excitations have been verified with the structure of stable solitons for condensed systems having attractive and repulsive interactions. In this regard, we note that the existence of solitons in BECs with SOC was investigated in Ref. [9], for the case in which there are repulsive interactions between atoms, and, in Refs. [10–13], when the interactions are attractive. Gap solitons are predicted in Ref. [14] for a BEC with SOC in a spatially periodic Zeeman field, corresponding to a linear optical lattice. Experimentally, it is not an easy task to control the SOC parameter, with recent suggestions to tune it by applying rapid time variations of the Raman frequency [15,16]. The experimental observations reported in Ref. [17] show that the spin-orbit coupling can be tuned in this way. In principle, the periodic variation in time of the condensate parameters can lead to new phenomena such as the generation of new quantum phases [18], artificial gauge fields [19], compacton matter waves [20], etc. Therefore, it is actually quite relevant and of interest to investigate how the periodic time variations of the Raman frequency can affect the nonlinear modes of the condensate, such as solitons and vortices. In the limit of high frequencies, as shown in Ref. [15], the averaged Hamiltonian contains the nontrivial renormalization of the spin-orbit coupling, as well as the new effective nonlinear phase, which is sensitive to the interaction strengths [21].

Our main task in the present work is to investigate the dynamics of solitons and Josephson-type oscillations between solitonic components, considering BECs with tunable spin-orbit coupling, with attractive interactions between the atoms, under slow and rapid time modulations of the Raman frequency. In this regard, related to Josephson oscillations in BECs, we note some previous studies in Refs. [22–25]. In particular, when considering the Raman frequency modulated in time together with changes in other parameters of the system, one should expect to observe parametric resonance phenomena occur in the internal Josephson oscillations, which have been introduced between the atom-number fraction existent in each of the components of the condensate with SOC. The parametric resonances in this case are introduced by the time dependence of the Raman frequency and its corresponding relation with spin-orbit coupling of the two components of the condensate. Such study can be useful for possible experimental investigations, which can help the control of BEC parameters through resonance phenomena observations. We should point out that previous studies of parametric resonances in BEC have been mainly concerned with time variations in trap configurations, optical lattices, as well as nonlinear parameters, looking for direct interference effects manifested in the densities [26–31]. In our present study, by introducing a time modulation in the Raman frequency, the main focus is the oscillatory behavior between the internal atom-number population of the two components during the time evolution of the condensate.

We start our study by first considering the case in which we have defined the spin-orbit parameter and constant Raman frequency in order to verify the characteristics of the existent

soliton solutions, which can be regular or striped solitons. Next, we introduce an adiabatic time modulation in the Raman frequency (growing and decreasing linearly), such that we can study how to switch between different kind of solitons. We follow our study by considering the Josephson oscillations between the components for both the cases in which we have regular and striped soliton solutions. Parametric resonance effects in the oscillations are verified by periodically considering time variation of the Raman frequency at some given SOC parameters. The case of rapid time modulations of the Raman frequency can be treated by using a time-averaging approach, which is implemented over the time-dependent coupled system, implying a renormalization of the SOC and nonlinear parameters. In this way, the interactions are effectively time independent. This case is discussed in Sec. IV.

We consider exact numerical simulations in all the cases, complemented by theoretical analysis, using variational approaches, whenever simplified solutions can be performed. As shown, the predictions derived by using the variational approach (VA) are verified to be fully consistent with the given numerical results in the region where regular bright solitons are obtained. In other cases, where the solutions are striped ones, demanding more parameters in the Ansatz, the VA is quite helpful to indicate regions of stability as well as the initial starting profiles for the full numerical computation. By using the multiscale expansion method for the averaged system, solitonic solutions are also found and confirmed by our numerical simulations of the full coupled system with time-dependent Raman frequency.

Next, the basic formalism of the model is presented in Sec. II. For reference to other sections, we add Sec. II A, where we provide some details of the linear energy dispersion, which defines two regions for the kind of soliton solutions that we can obtain (regular or striped). And in Sec. II B, we already include some results to exemplify the two possible solutions and how to transform solitons between the two regions by considering the adiabatic linear time variation of the Raman frequency. In Sec. III, by considering the Raman frequency modulated in time and Josephson oscillations, we analyze the possibility to obtain resonant responses. The case with the Raman having high-frequency modulations is presented in Sec. IV. Finally, in Sec. V, we present our main conclusion.

II. MODEL FORMALISM

In our approach, we consider a spin-orbit-coupled BEC with equal Rashba and Dresselhaus contributions for the spin-orbit-coupling terms, as in Ref. [11], which can be described by a one-dimensional (1D) coupled equation for the two pseudospin components. For that, let us consider a harmonic trap where the frequency along one direction, ω_x , is much smaller than the frequency in the perpendicular direction, ω_\perp . In this case, given the units of energy, length, and time, respectively, by $\hbar\omega_\perp$, $a_\perp = \sqrt{\frac{\hbar}{m\omega_\perp}}$, and $1/\omega_\perp$ (where m is the mass of both atomic components), we can write in dimensionless units the corresponding SOC formalism for the two pseudospin components, $u \equiv u(x,t)$ and $v \equiv v(x,t)$, of the total wave function,

$$\psi \equiv \psi(x,t) \equiv \begin{pmatrix} u \\ v \end{pmatrix}. \quad (1)$$

The corresponding matrix-formatted nonlinear Schrödinger-type coupled equation can be written as

$$i \frac{\partial}{\partial t} \begin{pmatrix} u \\ v \end{pmatrix} = \left[-\frac{1}{2} \frac{\partial^2}{\partial x^2} - ik_L \sigma_z \frac{\partial}{\partial x} + V_{\text{tr}} + \Omega(t) \sigma_x \right] \begin{pmatrix} u \\ v \end{pmatrix} - \begin{pmatrix} |u|^2 + \beta|v|^2 & 0 \\ 0 & \beta|u|^2 + \gamma|v|^2 \end{pmatrix} \begin{pmatrix} u \\ v \end{pmatrix}, \quad (2)$$

where $V_{\text{tr}} \equiv V_{\text{tr}}(x) \equiv (\omega_x/\omega_\perp)^2 x^2/2$ is the trap potential, assumed to be zero ($V_{\text{tr}} = 0$) in the present study. $\sigma_{x,z}$ are the usual Pauli matrices, with k_L being the strength of the spin-orbit coupling and $\Omega(t)$ the time-dependent Raman frequency (also given in units of the trap frequency ω_\perp). In the nonlinear terms we have the dimensionless parameters β and γ , which are given by the ratio between the two-body scattering lengths, a_{ij} ($i, j = 1, 2$), of the two atomic components, such that $\beta = |a_{12}/a_{11}|$, $\gamma = |a_{22}/a_{11}|$. In the present work, we are going to consider attractive two-body interactions, such that we have an overall minus signal for the nonlinear interaction. From the symmetry of the coupled equations (2) for $\gamma = 1$, we can extract a simple relation between the two components u and v : Let us consider that for a given parameter k_L , we are identifying the solution for u by $u(x,t) \equiv u_{(k_L)}(x,t)$. In this case, a particular solution decoupling the equations can be verified with $v(x,t) = \pm u_{(-k_L)}(x,t)$.

A. Linear energy spectrum

For a constant Raman frequency $\Omega(t) = \Omega_0$, the linear energy spectrum can be derived by considering a plane-wave function with momentum k , $(u, v) = (u_0, v_0) \exp\{i[kx - w(k)t]\}$, which will give us the following dispersion relation:

$$w_\pm(k) = \frac{1}{2}k^2 \pm \sqrt{k_L^2 k^2 + \Omega_0^2}. \quad (3)$$

This relation, also shown in Ref. [11], is plotted as a function of k in Fig. 1, where two different regions (I and II) can be distinguished according to the choice of parameters we have for the spin-orbit coupling k_L and Raman frequency Ω_0 .

In region I, which happens when $k_L^2 < \Omega_0$, we can only obtain two single minima in the dispersion relation: when $w_\pm(k) = w_\pm(0) = \pm\Omega_0$. For $k_L^2 > \Omega_0$, in region II, $w_+(k)$ has just one minimum (at $k = 0$, as in the case of region I). However, in this case, the dispersion relation for $w_-(k)$ presents a local maximum at $k = 0$ with two minima at $k = \pm k_0$, where $k_0 \equiv k_L \sqrt{1 - \Omega_0^2/k_L^4}$; both with $w_{\text{min}} = k_0^2/2 - k_L^2 = -(k_L^2 + \Omega_0^2/k_L^2)/2$.

As already verified in Ref. [11], bright-soliton solutions of the nonlinear Schrödinger equation (NLSE) are obtained in region I. However, for $k_L^2 > \Omega_0$ (region II), the solutions are striped-type bright solitons. In Fig. 1, the two regions are represented and exemplified for particular values of Ω_0 , $= 2k_L^2$ (region I) and $= 0.3k_L^2$ (region II). The bright-solitonic solutions can be found by the multiple-scale analysis, which is used in Sec. IV to investigate the soliton dynamics under rapid modulations of parameters. Here, we should remark that the observation of striped phases has been recently reported in Ref. [5] for a BEC with SOC. In the following section, we exemplify the kind of soliton solutions we obtain in both regions, using constant and linearly time-varying Raman frequencies.

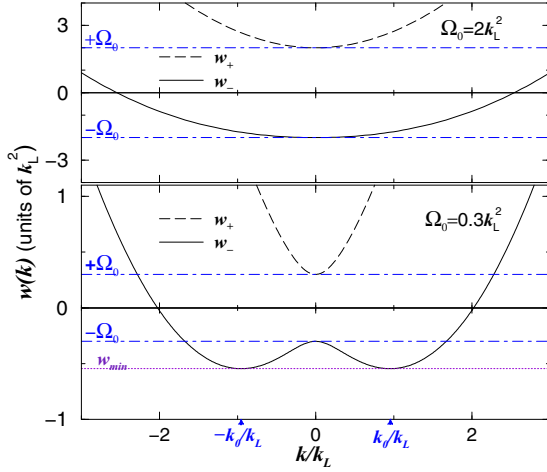


FIG. 1. Energy dispersions $w_+(k)$ (dashed curves) and $w_-(k)$ (solid curves), given by (3), are shown for two regions of parameters: region I, when $k_L^2 < \Omega_0$ (upper panel, exemplified with $\Omega_0 = 2k_L^2$), and region II, when $k_L^2 > \Omega_0$ (lower panel, exemplified with $\Omega_0 = 0.3k_L^2$). In both panels, the dot-dashed and dotted lines indicate the extremes, with the minima of w_+ at $(k, w_+) = (0, \Omega_0)$. The minima of w_- are at $(k, w_-) = (0, -\Omega_0)$ in region I and at $(\pm k_0, w_{\min})$ in region II, where $k_0^2 = k_L^2 - \Omega_0^2/k_L^2$ and $w_{\min} = -k_L^2 + k_0^2/2$.

B. Regular and striped soliton interchanged by adiabatic time variation of $\Omega(t)$

With adiabatic time variation of the Raman frequency, $\Omega(t)$, we can transform solitons from one region to another region for a given fixed k_L . By considering a regular soliton obtained in region I for $\Omega(t) = \Omega_0$, it can be transformed to a striped soliton by decreasing $\Omega(t)$, or, the other way, if started in region II. For that, let us consider a variation of the form

$$\Omega(t) = \Omega_0(1 \pm \Delta t). \quad (4)$$

Recently, such variation has been used in numerical simulations for dark-soliton generations in a BEC with SOC [32]. The transition of a soliton solution obtained in region II (striped soliton) to region I (regular soliton), and back from region I to region II, is illustrated in Fig. 2, obtained for different values of the time-dependent Raman frequency such that we have an adiabatic transition. In terms of the step function $\Theta(x)$ ($=0$ or 1 , respectively, for $x < 0$ or $x \geq 0$), we can write the time-varying Raman frequency as $\Omega(\tau) = (45 + \tau)\Theta(20 - \tau) + (85 - \tau)\Theta(\tau - 20)$. In these cases, the results are obtained with the same values of the nonlinear parameters, which are related to the scattering length ratios, $\beta = \gamma = 1$, implying that the inter- and intraspecies scattering lengths remain the same.

In all the cases considered in the present work, we are using exact full-numerical solutions of the coupled Gross-Pitaevskii (GP) formalism (2) by applying an imaginary-time propagation method [33] using the Crank-Nicolson algorithm, followed by real-time evolution of the soliton profiles. The time steps, as well as the total x -space interval and corresponding discretization, have been adapted to obtain convergent and accurate results. In most of the cases, considering our dimensionless units, we found the time step $\delta t = 10^{-3}$ to be sufficient in the imaginary-time relaxation procedure and 10^{-4} in the real-time

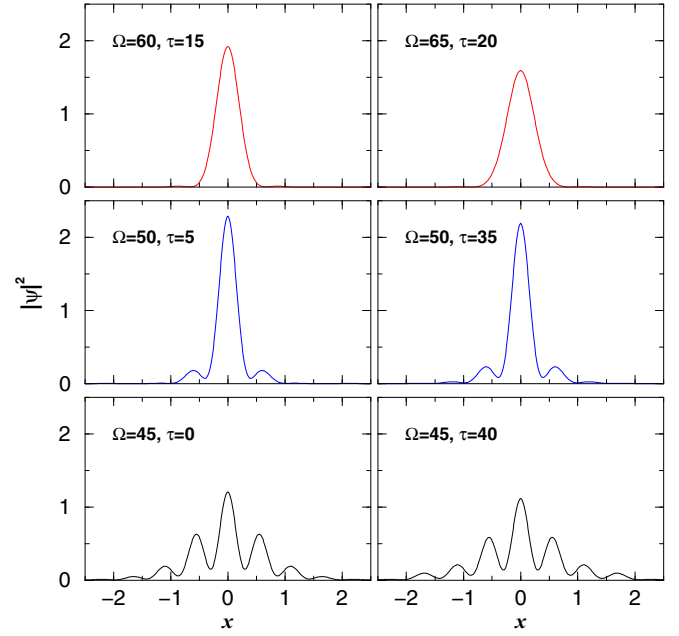


FIG. 2. A soliton profile is shown for $\Omega(t)$ varying in time as $\Omega(\tau) = (45 + \tau)\Theta(20 - \tau) + (85 - \tau)\Theta(\tau - 20)$ [where $\Theta(x) = 0$ for $x < 0$, and 1 for $x \geq 0$]. The parameters are $k_L = 8$, $\beta = 1$, and $\gamma = 1$. The soliton is generated as a striped one (region II, lower-left panel with $\Omega = 45$) being converted to a regular soliton (region I, in the upper-right panel with $\Omega = 65$), returning to region II by inverting the time variation. All quantities are dimensionless.

evolution. In this regard, we can mention that particular care has to be taken in the time evolution of striped solitons, where stable solutions demand a large enough number of grid points δx within a large x interval (to avoid border effects). In view of that, for some results we decrease the time step to $\delta t = 10^{-5}$. Throughout the text, we provide some theoretical analysis by using variational Ansätze, which are verified to be more efficient in region I where the solutions are regular solitons. For the case in which rapid modulations are used for the Raman frequency, in region II, it was also shown to be quite useful to employ a multiscale expansion for the averaged coupled system.

III. TIME-MODULATED RAMAN FREQUENCY AND INTERNAL JOSEPHSON OSCILLATIONS

An interesting case that can be explored is the influence of time-varying Raman frequency on the oscillations in atomic populations, which can occur between the components of the soliton solutions (the internal Josephson effect) in regions I and II. The time-periodic modulation of the Raman frequency may lead to resonant responses of solitons in BECs with SOC. This phenomenon is possible to occur for the imbalanced populations between soliton components, which are produced initially with different phases. To study the dynamics of this kind of process, in both the cases of region I ($\Omega_0 > k_L^2$) and region II ($\Omega_0 < k_L^2$), we first implement the Josephson oscillations for constant Raman frequencies Ω_0 by introducing a phase between the two soliton components before starting the time evolution of the coupled system.

For the time-modulated Raman frequency, we consider the following expression:

$$\Omega(t) = \Omega_0 + \Omega_1 \cos(\omega t), \quad (5)$$

where Ω_1 is the amplitude, with ω the frequency of the oscillations. Different regimes are possible in the dependence of the values of the modulating frequency ω , such that we can have slow ($\omega \ll \Omega_0$), resonant ($\omega \sim \Omega_0$), or rapid ($\omega \gg \Omega_0$) modulations. In this section, we are mainly concerned with the intermediate regime, where we can have resonant responses such that we assume small amplitude for the oscillations, $\Omega_1 \ll \Omega_0$. The case of very slow frequency was reported in the previous study presented in Sec. II B. The other regime for the time-perturbed Raman, with high frequencies ω and large amplitudes Ω_1 , is considered in Sec. IV.

The studies in this section are done using a full-numerical simulation, as well as by some analytical considerations through a variational procedure. In order to study the interference effect on the Josephson oscillation due to a time-modulated Raman frequency, we employ a variational approach in region I (where $k_L^2 < \Omega_0$ and regular soliton solutions are obtained), considering the Ansatz

$$\begin{pmatrix} u \\ v \end{pmatrix} = \begin{pmatrix} A_1 e^{-[(x-x_0)^2/(2a^2) - ik_1 x - i\phi_1]} \\ A_2 e^{-[(x-x_0)^2/(2a^2) - ik_2 x - i\phi_2]} \end{pmatrix}, \quad (6)$$

where A_i , a , x_0 , k_i , and ϕ_i ($i = 1, 2$) are time-dependent parameters where we have the assumption that the solitons have the same width a and center of mass x_0 (i.e., both components overlap), which are confirmed by numerical simulations. By considering the Lagrangian density for Eq. (2) and the above variational Ansatz, we have

$$\begin{aligned} \mathcal{L}(x, t) = & \left[\frac{i}{2} \left(u^* \frac{du}{dt} + v^* \frac{dv}{dt} \right) \right. \\ & \left. + \frac{ik_L}{2} \left(u^* \frac{du}{dx} - v^* \frac{dv}{dx} \right) + \text{c.c.} \right] \\ & - \frac{1}{2} \left| \frac{du}{dx} \right|^2 - \frac{1}{2} \left| \frac{dv}{dx} \right|^2 - \Omega u^* v - \Omega v^* u \\ & + \frac{1}{2} |u|^4 + \frac{\gamma}{2} |v|^4 + \beta |u|^2 |v|^2, \end{aligned} \quad (7)$$

with the Lagrangian given by $L = \int_{-\infty}^{\infty} dx \mathcal{L}(x, t)$:

$$\begin{aligned} L = & - \sum_{i=1}^2 N_i \left[\frac{d\phi_i}{dt} + \frac{dk_i}{dt} x_0 + \frac{1}{4a^2} + \frac{k_i^2}{2} + (-)^i k_i k_L \right] \\ & - 2\Omega(t) \sqrt{N_1 N_2} e^{-a^2 k^2} \cos(2k_- x_0 + \phi) \\ & + \frac{1}{2\sqrt{2\pi} a} (N_1^2 + \gamma N_2^2 + 2\beta N_1 N_2). \end{aligned} \quad (8)$$

Here, and in the following, we use the definitions $k_{\pm} \equiv (k_1 \pm k_2)/2$ and $\phi \equiv \phi_1 - \phi_2$. The number of atoms for each component $i = 1, 2$ is given by $N_i \equiv \sqrt{\pi} A_i^2 a$, with the total number $N = N_1 + N_2$ being conserved. By assuming a weak SOC parameter, $k_- \approx k_L$, following arguments given in Ref. [34], the corresponding Euler-Lagrange equations for the

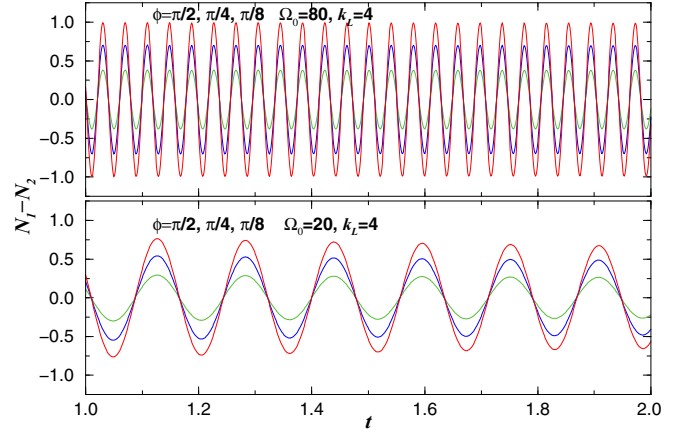


FIG. 3. The atom-number oscillations, with the corresponding dependence on the phase ϕ introduced between components for solitons in region I, are shown for $\Omega_0 = 80$ (upper panel) and 20 (lower panel). The given results are for $\phi = \pi/8$ (green, smaller amplitudes), $\pi/4$ (blue, intermediate amplitudes), and $\pi/2$ (red, larger amplitudes), with the spin-orbit coupling and nonlinear parameters, respectively, given by $k_L = 4$ and $\gamma = \beta = 1$. All quantities are in dimensionless units.

parameters are given by

$$\begin{aligned} \frac{dx_0}{dt} &= k_+, \\ \frac{dk_+}{dt} &= 2e^{-k_L^2 a^2} \Omega(t) k_L \sqrt{1 - Z^2} \sin(\varphi), \\ \frac{dZ}{dt} &= -2e^{-k_L^2 a^2} \Omega(t) \sqrt{1 - Z^2} \sin(\varphi), \\ \frac{d\varphi}{dt} &= 2k_L k_+ + \Lambda Z + \frac{2e^{-k_L^2 a^2} \Omega(t) Z}{\sqrt{1 - Z^2}} \cos(\varphi), \end{aligned} \quad (9)$$

where $Z \equiv (N_1 - N_2)/N$, $\varphi \equiv 2k_- x_0 + \phi$, $\Lambda \equiv N(1 - \beta)/(\sqrt{2\pi} a)$, and, for simplicity, we fix $\gamma = 1$. In the case of a hyperbolic-type Ansatz, the exponential factor in the above equations, derived from a Gaussian Ansatz, is changed as $e^{-k_L^2 a^2} \rightarrow (\pi k_L/\eta)/\sinh(\pi k_L/\eta)$ (where η is the soliton amplitude). In the weak SOC limit, when $k_L \ll \eta/\pi$ or $k_L \ll 1/a$, this factor reduces to one.

This system is analogous to the one considered in [34] for a constant $\Omega = \Omega_0$, where it was shown that in the Euler-Lagrange system for the parameters, the equation for the center of mass, $x_0 = (x_1 + x_2)/2$, can be approximately solved as $x_0 \approx (k_L/2\Omega_0) \cos(2\Omega_0 t)$. Thus, the center-of-mass oscillations are small, with its amplitude of the order of $\approx k_L/2\Omega_0$. By considering our numerical simulations, as discussed in more detail in the next section and with results given in Figs. 3 and 4, for the case that $k_L = 4$ and $\Omega_0 = 20$, we have confirmed that the center-of-mass oscillations agree with the estimated value of ~ 0.1 , as shown in Fig. 4.

Then, for small values of k_L (as compared with Ω_0), we can consider the following coupled system:

$$\frac{d\phi}{dt} = \Lambda Z + \frac{2e^{-k_L^2 a^2} \Omega(t) Z}{\sqrt{1 - Z^2}} \cos(\phi), \quad (10)$$

$$\frac{dZ}{dt} = -2e^{-k_L^2 a^2} \Omega(t) \sqrt{1 - Z^2} \sin(\phi), \quad (11)$$

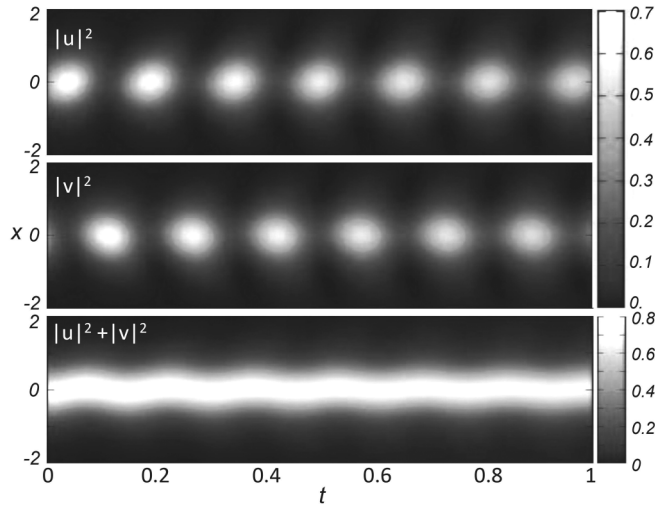


FIG. 4. Density plots for soliton profiles corresponding to the lower panel of Fig. 3 ($\Omega_0 = 20$) for $|u(x,t)|^2$ (upper panel), $|v(x,t)|^2$ (middle panel), and $|u(x,t)|^2 + |v(x,t)|^2$ (lower panel), obtained at the positions x in the time interval $0 \leq t \leq 1$. The density levels are indicated in the right-hand side (all quantities are dimensionless).

which describes the internal Josephson oscillations of atomic populations between two pseudospin components. For a constant Raman frequency, these oscillations have been studied in Ref. [35]. It appeared when investigating the macroscopic quantum tunneling obtained in a double-well potential having a barrier between the wells with constant height [36]. This was also studied in Refs. [37–39] for the case in which the barriers between wells have their heights oscillating in time.

At some frequencies of the modulations, it is possible to verify parametric resonance in the Josephson oscillations. In the following, we will discuss the full-numerical results by considering the two possible regions defined in Fig. 1 by the relations between the Raman and SOC parameters. The results obtained in region I, where we have bright-type solitons, are shown to be fully compatible with a variational approach. However, for region II, where we have striped soliton solutions, the coupled system is not so amenable to simplified variational analysis such that we can provide only rough estimates for some limiting situations. Therefore, in the case of time evolution for the striped solitons with constant and time-dependent Raman frequencies, our study relies mostly on full-numerical simulations, which are shown to provide convergent results with high numerical precision.

A. Results for Josephson oscillations in region I

The results in this case are for $\Omega_0 > k_L^2$, considering the Raman frequency constant as well as time modulated. In the case of time-modulated Raman frequency, we also have introduced a variational analysis to provide an estimate for the localization of the modulation frequency leading to the resonant behavior.

1. Constant Raman frequency: $\Omega(t) = \Omega_0$

When Ω_0 is constant, the frequency of the free oscillations is given by

$$\omega_J = \sqrt{2\Omega_0(2\Omega_0 + \Lambda)} \quad (=2\Omega_0 \text{ for } \beta = 1). \quad (12)$$

From numerical simulations for free Josephson oscillations of the full system of the GP equation, the results obtained in region I ($k_L^2 > \Omega_0$) are represented in Figs. 3 and 4 by considering the spin-orbit-coupling parameter $k_L = 4$, with two constant Raman frequencies given by $\Omega_0 = 80$ (upper panel) and $\Omega_0 = 20$ (lower panel). In Fig. 4, we show the density plots for $|u|^2$, $|v|^2$ and $|u|^2 + |v|^2$, corresponding to the case in which $\Omega_0 = 20$ for the time interval $0 < t < 1$.

The purpose, in this case, is to verify the dependence of the oscillating behavior on different values of the initial phase ϕ introduced between components when starting the evolution. By considering three values for the initial phase ϕ , it is shown that the maximum of the periodic atom transfer occurs at $\phi = \pi/2$, reaching almost 100% of atoms in the case in which $\Omega_0 = 80$. It is also shown that the phase ϕ affects only the amplitude of the oscillations, but not the frequency. The constant Raman parameter will determine the frequency of the oscillations, which is given by $\approx 2\Omega_0$, confirming the theoretical prediction (12).

2. Time-modulated Raman frequency: $\Omega(t) = \Omega_0 + \Omega_1 \cos(\omega t)$

Now, let us analyze the case when $\Omega(t)$ is modulated in time such that $\Omega(t) = \Omega_0 + \Omega_1 \cos(\omega t)$, in order to verify the localization of possible resonant behaviors. For that, we can consider two limiting conditions for Eq. (10): one applied for $Z \ll 1$, when $\phi(0) \approx 0$, and the other for the regime of macroscopic quantum localization, as follows.

Let us consider the linear regime case, when $\phi(0) \approx 0$ and $Z \ll 1$. Within these conditions in Eq. (10), using the second derivative for Z , we obtain a modified Mathieu differential equation with the main term in Z oscillating with a frequency ω_0 , where $\omega_0^2 \equiv 2\Omega_0(2\Omega_0 + \Lambda) + (2\Omega_1)^2$. For that, when considering small values of Λ and Ω_1 , the standard analysis as given in Ref. [40] can be applied, which leads to a resonance at $\omega = 2\Omega_0$ (in case $\beta = 1$, so $\Lambda = 0$). In this case, parametric resonances are also expected to occur for $\omega = 2\omega_J$, where ω_J is the frequency of free Josephson oscillations given in Eq. (12).

The results of our investigations on resonant interferences which can occur in region I are presented in Figs. 5–8. They are obtained from numerical simulations of the full coupled system (2), with the Raman and SOC parameters $\Omega_0 = 320$ and $k_L = 8$, respectively. For the time modulation of the Raman parameter, given by Eq. (5), we assume the amplitude given by $\Omega_1 = 0.1\Omega_0$. The choice of these parameters in region I is to more clearly distinguish the manifestation of resonant interferences in the Josephson oscillations between the atom numbers of the two components, $Z = N_1 - N_2$ ($N = 1$). We also found it illustrative to provide some density plots for the components and total profiles corresponding to the results presented in Fig. 5. Therefore, in Fig. 6, we show the case where we have $\beta = 0$ in Fig. 5. Here, we should remark that the perturbed results obtained when we are not close to the resonant interference regions are shown to be almost identical to the unperturbed results (as observed by comparing the first column of panels in Fig. 6 with the third column). Indeed, quite small center-of-mass oscillations are verified near the initial localization. Another point that can be observed from these results is that the center of mass of the soliton is strongly affected by the resonant behavior,

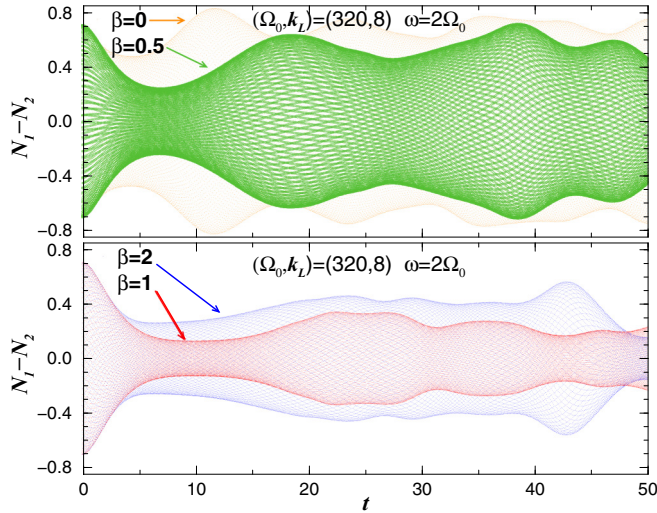


FIG. 5. Resonant interference patterns verified for $\omega = 2\Omega_0$ are shown in the atom-number oscillations for the case in which $\Omega_0 = 320$, $\Omega_1 = 0.1\Omega_0$, $k_L = 8$, and $\gamma = 1$, considering different values of parameter β (as indicated by the corresponding arrows). We have $\beta = 0$ and 0.5 in the upper panel, and $\beta = 1$ and 2 in the lower panel. The shaded areas, in each case, represent the range of the oscillations in the real-time propagation of the two components. In all these cases, the time evolution was performed with $\delta t = 10^{-4}$, with a starting phase $\pi/4$ introduced between the two components. All quantities are in dimensionless units.

such that it can be verified in the central panels of Fig. 6 that the central position is moving from $x = 0$ at $t = 0$ to $x \approx 2$ at $t = 16$. There is no change observed in the center of mass for the other cases, outside the resonant region. The

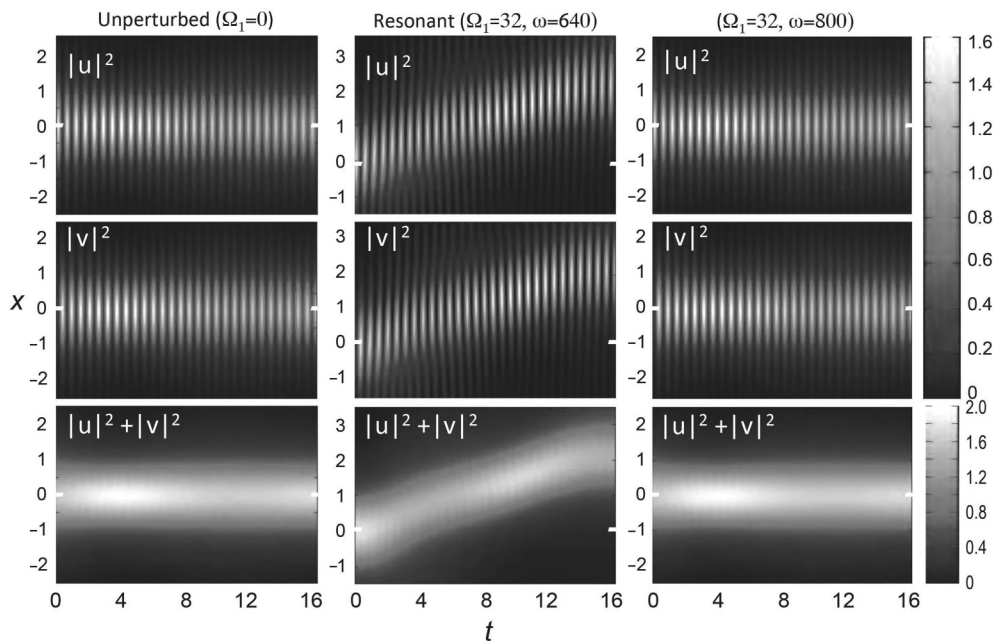


FIG. 6. Density plots for soliton profiles corresponding to the case with $\beta = 0$ shown in Fig. 5 ($\Omega_0 = 320$) for $|u(x,t)|^2$ (upper panels), $|v(x,t)|^2$ (middle panels), and $|u(x,t)|^2 + |v(x,t)|^2$ (lower panels), obtained at the positions x in the time interval $0 \leq t \leq 16$. In the left frames, we have the nonperturbed oscillations ($\Omega_1 = 0$); in the middle frames, the oscillations at resonant position ($\Omega_1 = 0.1\Omega_0 = 32$, with $\omega = 2\Omega_0$); and, in the right frames, the nonresonant perturbed case, with $\omega = 2.5\Omega_0$. All quantities are in dimensionless units.

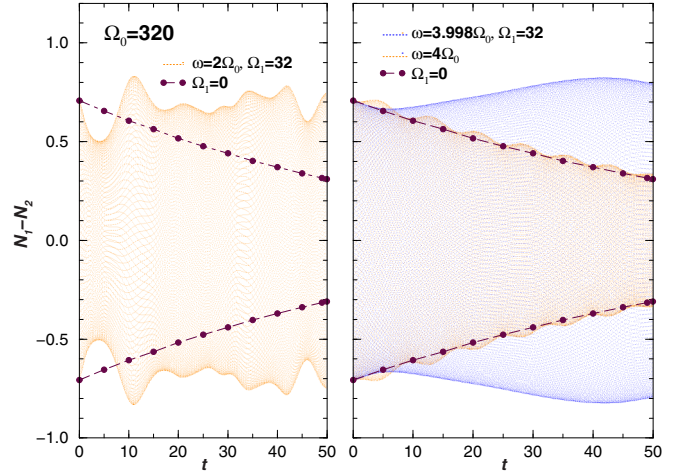


FIG. 7. Parametric resonant behaviors verified in the atom-number oscillations $N_1 - N_2$ during the time propagation of a two-component soliton, with $\Omega_0 = 320$, $k_L = 8$, $\Omega_1 = 0.1\Omega_0$, $\beta = 0$, and $\gamma = 1$. In both panels, we also indicate with dash-dotted lines the extremes of the oscillations for the case $\Omega_1 = 0$, for comparison. In the left panel, the oscillations at resonant position, $\omega = 2\Omega_0$, are within the shaded region. In the right panel, we show the results for two frequencies ($\omega = 4\Omega_0$ and $\omega = 3.998\Omega_0$) close to the region where parametric resonance is expected. The shaded region with oscillations close to the nonperturbed case is for $\omega = 4\Omega_0$. In all these cases, for the time interval shown, the time step was $\delta t = 10^{-5}$, with a starting phase $\pi/4$ introduced between the two components. All quantities are in dimensionless units.

numerical simulations of the variational system (8) confirm this behavior of the motion of the center of mass for the solitonic

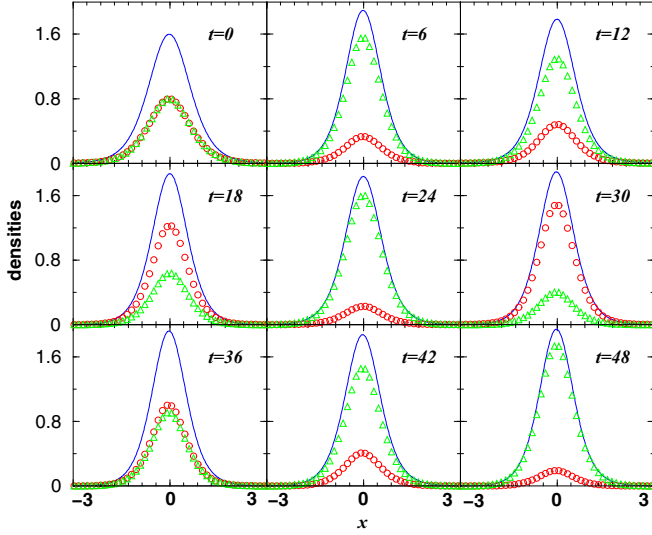


FIG. 8. Density profiles $|\psi|^2$ (solid blue), $|u|^2$ (red circles), and $|v|^2$ (green triangles) for different time positions in the evolution of the coupled soliton, considering the case shown in the right panel of Fig. 7, where $\omega = 3.998\Omega_0$. The parameters are $k_L = 8$, $\Omega_0 = 320$, $\Omega_1 = 0.1\Omega_0$, $\beta = 0$, and $\gamma = 1$, with a starting phase $\pi/4$. All quantities are in dimensionless units.

components and the oscillations of the atomic imbalance at the resonance.

We should comment that for the values of the frequency ω , the resonant position (“window”) is quite sharp, as verified in our numerical simulation, such that the resonant perturbations are confirmed only for ω very close to 2 and 4 Ω_0 , which makes the simulations quite time demanding. As shown in Fig. 5 and in the left panel of Fig. 7, for a large time interval going up to $t = 50$, one of the resonant positions is detected for $\omega = (2 \pm 0.001)\Omega_0$. By a slightly larger deviation of this frequency, the results for the oscillations are about the same as given for the nonperturbed case ($\Omega_1 = 0$), shown in the left panel of Fig. 7. The other resonant position, as shown in the right panel of Fig. 7, for $\beta = 0$, is found in an even smaller range of ω , given by $\omega = 3.998\Omega_0$, with the fluctuation starting to appear when we have ω exactly $4\Omega_0$. In Fig. 5, we also show how the resonant behaviors are affected by changes in the nonlinear parameter β . As shown, it is enhanced in the case that $\beta = 0$, with the variation $N_1 - N_2$ having peaks with maxima close to 0.9. The case of $\beta = 0$, for $\omega = 2\Omega_0$, is also presented in the left frame of Fig. 7 for comparison with the unperturbed results of the Josephson oscillations.

With Fig. 8, we conclude the analysis of the results shown in Figs. 5–7 by presenting the behaviors of density profiles (total and for each component) in two-dimensional plots for different time positions of the evolution.

B. Results for Josephson oscillations in region II

Now, let us consider the Josephson oscillations between components of the striped soliton solutions, corresponding to region II in the dispersion relation, which are given by $\Omega_0 < k_L^2$. We perform this study by considering full-numerical

simulations of the corresponding GP coupled equations. First, we provide some results obtained for Josephson oscillations in the case in which we have constant Raman frequency. Next, we consider the more general case, where the Raman frequency is modulated in time, and we can have resonant results at some particular values of the modulating frequency ω .

We start the study of this section by considering a variational analysis, where we need to introduce the momentum $k_0 = \pm k_L \sqrt{1 - \Omega_0^2/k_L^4}$, which provides the momentum position of the minima shown in the lower panel of Fig. 1. By observing that the coupled equations for the imbalanced populations and relative phase are not easy to derive in explicit form, in a more general case, let us assume that the tunneling between components occurs for the same sign of k_0 . The time modulations for $\Omega(t)$ are not inducing transitions between oppositely propagating modes with $\pm k_0$. To have such transitions, the so-called momentum Josephson oscillations, we need parameters with periodic modulation in space [41]. Therefore, by assuming for the components the same Ansatz as given in Eq. (6) but with $k_{i=1,2} = k_0$ and considering the center fixed at $x = 0$, we arrive at the same coupled expressions (10) and (11), except that the equation for $d\phi/dt$ contains an additional term $2k_L k_0$. By linearizing the system relative to Z , we obtain

$$\frac{d\phi}{dt} = 2k_L k_0 + [\Lambda + 2\Omega(t)]Z \cos(\phi), \quad (13)$$

$$\frac{dZ}{dt} = -2\Omega(t) \sin(\phi). \quad (14)$$

For a constant Ω and with $2k_L k_0 \gg \Lambda + 2\Omega_0$, we have

$$\phi \approx \phi_0 + (2k_L k_0)t, \quad (15)$$

implying that the population imbalance Z is oscillating with the frequency $\omega_{\text{str}} \approx 2k_L k_0$. Therefore, we should expect a different behavior of the results, in comparison with the region I, in the initial stage (defined by $k_L k_0$). For larger time of the propagation, the frequency for the oscillations should approach the same ones as verified for region I.

1. Constant Raman frequency: $\Omega(t) = \Omega_0$

For the numerical simulation of the Josephson oscillations obtained in region II, we first select some results obtained for constant values of Ω_0 , which are given in Figs. 9 and 10, by considering an initial phase difference between components given by $\pi/2$. In these cases, by considering $k_L = 4$ (Fig. 9) and $k_L = 8$ (Fig. 10), with several values of $\Omega_0 < k_L^2$, we can clearly verify that we have an initial stage of the oscillations where the frequencies are not depending on Ω_0 , but only on the values of k_L , being $\omega \sim 10\pi$ for $k_L = 4$ and $\omega \sim 40\pi$ for $k_L = 8$. The values of Ω_0 affect only the amplitude of the initial oscillations. However, for larger times, the behavior of the frequencies is similar to region I. Another observation from these results is that for a long-time interval, the Josephson oscillations are being damped as we increase the difference $k_L^2 - \Omega_0$. In Fig. 10, we present two inset panels from which

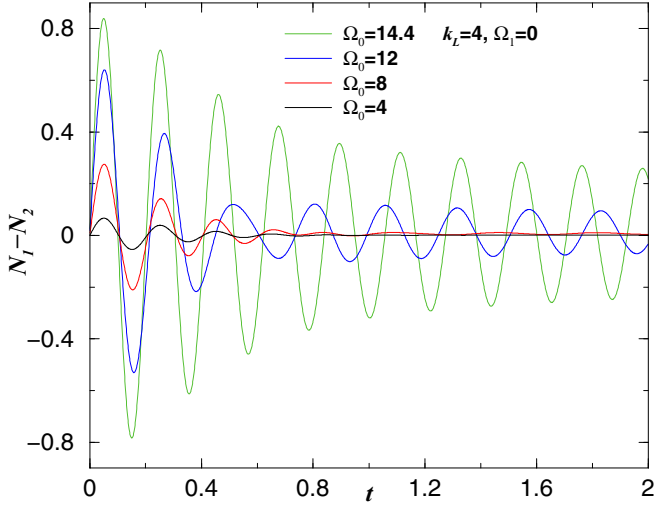


FIG. 9. Atom-number oscillations between components are shown as functions of time, for $k_L = 4$ in region II, where larger initial amplitudes correspond to larger values of Ω_0 (indicated inside the panel). As verified, the amplitude of the oscillations decays faster for smaller values of Ω_0 . The initial phase is $\phi = \pi/2$ (to enhance the amplitude of the oscillations), with $\beta = \gamma = 1$. All quantities are dimensionless.

we can verify the initial and intermediate oscillation patterns. In the inset with $t \leq 0.2$, just after starting the evolution, the frequency is about the same for all three cases, $\omega \sim 40\pi$, not depending on Ω_0 . In the other inset, for $0.2 \leq t \leq 0.4$, after a

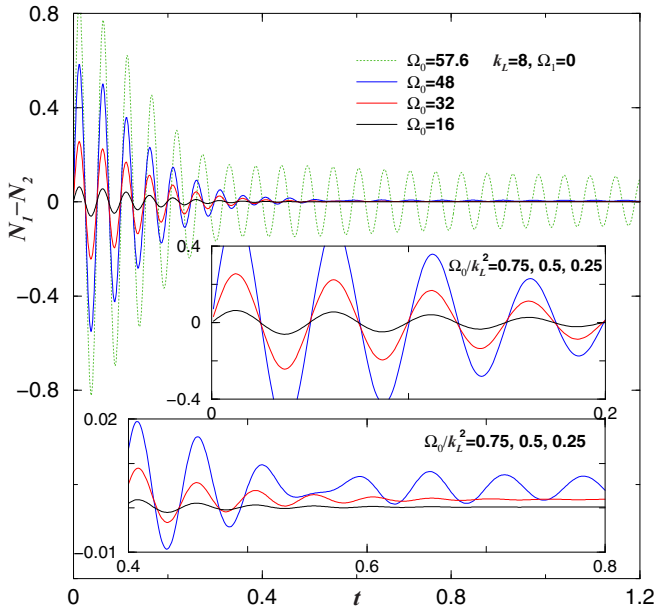


FIG. 10. Atom-number oscillations between components are shown as functions of time, for $k_L = 8$ in region II, for few values of Ω_0 (indicated inside the panels). As in Fig. 9, larger initial amplitudes correspond to larger values of Ω_0 . The two inset panels are given in appropriate scales to clarify the change in the oscillating behavior in two time intervals. As in Fig. 9, here the initial phase was fixed at $\phi = \pi/2$, with $\beta = \gamma = 1$. All quantities are dimensionless.

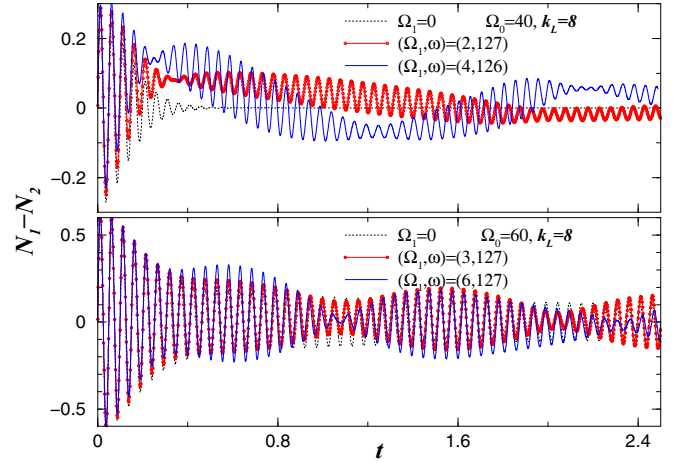


FIG. 11. Resonant interferences in the atom-number oscillations are shown for striped solitons for $k_L = 8$, $\beta = \gamma = 1$ and initial phase $\pi/4$. In the upper panel, we have $\Omega_0 = 40$, with $\Omega_1 = 2$ (red circles line) and 4 (blue solid line) compared with the unperturbed case $\Omega_1 = 0$ (black dotted line). In the lower panel, for $\Omega_0 = 60$ closer to k_L^2 , we have $\Omega_1 = 3$ (red circles line) and 6 (blue solid line) compared with the case $\Omega_1 = 0$ (black dotted line). In both cases, the resonant interferences are verified for $\omega \sim 40\pi$. All quantities are in dimensionless units.

transient time interval, the frequency changes to $2\Omega_0$ (as in the case of region I).

2. Time-modulated Raman frequency: $\Omega(t) = \Omega_0 + \Omega_1 \cos(\omega t)$

When studying the phase dependence of the atom-number oscillations for striped soliton solutions, we first observe that the amplitude of the oscillations depends on the initial phase difference, as already verified in the case in which we have a constant Raman frequency parameter, given by Ω_0 . Therefore, before considering the case where we have the Raman frequency perturbed in time, we have studied the phase dependence of the atom-number oscillations for striped soliton solutions during time evolution. In this numerical study, we have verified that for arbitrary initial fixed phase ϕ (from 0.01 to $\pi/2$) introduced between components, only the amplitude of the oscillations is being affected, which is verified by the transient time just after starting the evolution of the solutions. The frequency of the oscillations does not depend on the strength of the Raman frequency Ω_0 , at least during the transient time until the oscillations become stable. In a longer-time interval, after the transient time, the frequency of the oscillations will correspond to the Raman frequency, given by $2\Omega_0$, as discussed for the case of regular soliton solutions. As the initial phase between the components can be arbitrary and will not affect the natural frequency of the oscillations between N_1 and N_2 , when studying time-perturbed Raman frequency, in general, we choose this phase to be $\pi/4$ such that the amplitude of the natural oscillations is not too large and not too small.

In the case of periodic modulations of $\Omega(t)$ in region II ($\Omega_0 < k_L^2$), the results of our numerical simulations to identify parametric resonances is first exemplified by Figs. 11 and 12. In Fig. 11, for $k_L = 8$, we present two panels considering

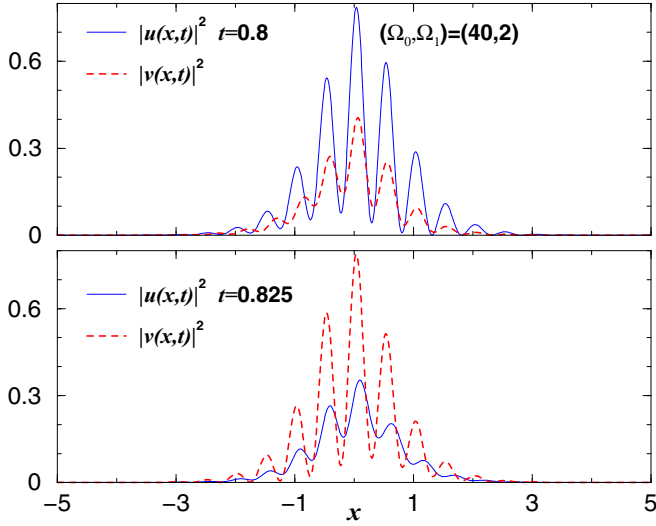


FIG. 12. Dynamics of the density oscillations between components for striped solitons are represented by two static panels: In the upper panel, the densities $|u(x,t)|^2$ and $|v(x,t)|^2$ are given for a fixed instant of time $t = 0.8$, with the lower panel given for $t = 0.825$, where the period of oscillations is about 0.05 (as verified from Fig. 11). The corresponding values of Ω_0 and Ω_1 are indicated inside the panels. The other parameters are such that $\beta = \gamma = 1$, $k_L = 8$. All quantities are in dimensionless units.

$\Omega_0 = 40$ (upper) and 60 (lower). In both, we are plotting the perturbed case considering the amplitude of the oscillations given by $\Omega_1 = 0.05\Omega_0$ and $0.1\Omega_0$, with the frequency $\omega \approx 2\pi \times$ the linear frequency verified in the transient time interval (~ 126 – 127). The nonperturbed case ($\Omega_1 = 0$) is also shown for comparison in both cases. We should emphasize that in general, the Josephson oscillating behavior is about the same as for the unperturbed case $\Omega_1 = 0$, except close to the specific values for ω and Ω_1 where resonant interference behaviors are detected. With Fig. 12, for a time interval of a half period of the Josephson oscillations, we represent the profiles of the two component densities [$|u(x,t)|^2$ and $|v(x,t)|^2$] for the case shown in the upper panel of Fig. 11 with $\Omega_0 = 40$ and $\Omega_1 = 2$ (the other parameters are the same). The oscillation dynamics is represented in two panels, given for $t = 0.8$ (upper panel) and $t = 0.825$ (lower panel), considering that a complete period is close to ≈ 0.05 . The panels indicate (through the corresponding densities) the atom-number oscillation between the components

For a long-time interval, resonant behaviors are expected to occur when considering cases where the natural frequency of the oscillations is still surviving in the unperturbed case. For that, in Fig. 13, we are showing results for a simulation with $k_L = 4$ and $\Omega_0 = 10$, with $\beta = 0.5$ and initial phase $\pi/8$. In this case, by taking $\Omega_1 = 4$, we can observe a resonant interference that occurs for $\omega_1 \sim 2\Omega_0$. For this case, the striped soliton profiles of both components are also represented in the two lower panels of the figure. In the left panel, we have them at $t = 0$, and in the right panel, for $t = 8$.

To conclude our study related to striped solitons and resonant interference effects, we present results obtained in long-time intervals for the case in which the unperturbed

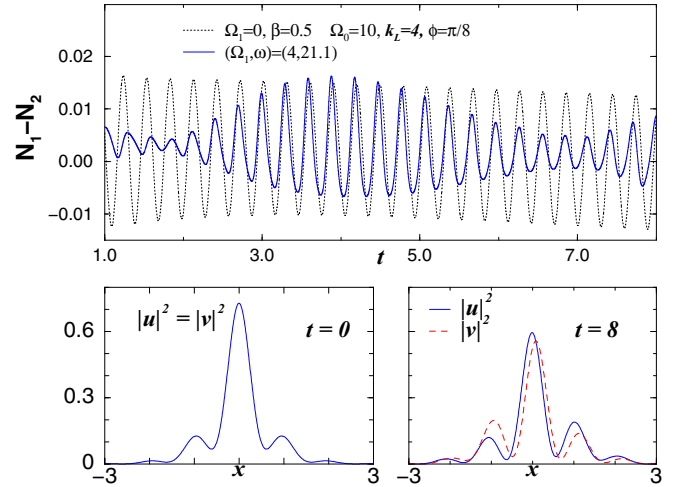


FIG. 13. Atom-number oscillations, $N_1 - N_2$ (upper panel), for striped solitons obtained in region II, for $k_L = 4$, $\Omega_0 = 10$, with corresponding resonant behavior that occurs at $\omega = 21.1$. In the two lower panels, we show the densities for the two components at $t = 0$ and $t = 8$, where the second case shows the effect of the time perturbation that was introduced. The other parameters are $\gamma = 1$, $\beta = 0.5$, and the initial phase $\phi = \pi/8$. All quantities are dimensionless.

Raman is given by $\Omega_0 = 10$, with $k_L = 4$, as in Fig. 13, but with a much smaller amplitude of the modulations such that $\Omega_1 = 0.05\Omega_0$. The investigation of the interval of ω where interferences can be found is shown in Fig. 14, considering a small initial phase of oscillations between components given by $\phi = \pi/8$. As shown by the set of five panels (for $1 \leq t \leq 8$) with given values of ω , resonant interference effects due to the

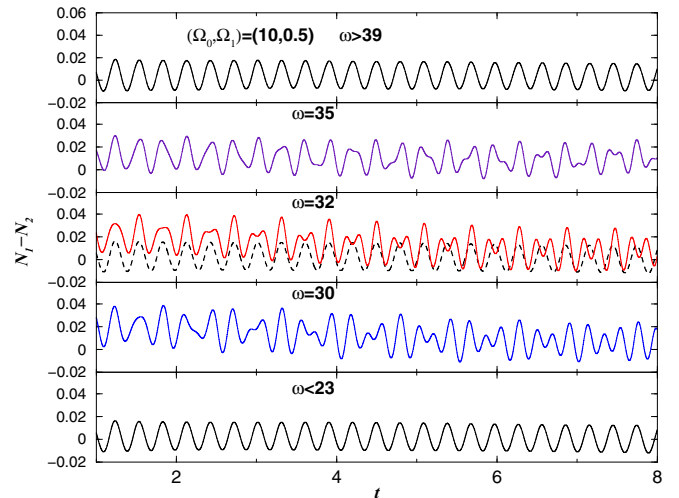


FIG. 14. Atom-number oscillations, $N_1 - N_2$, for striped solitons in region II, for $k_L = 4$ and $\Omega_0 = 10$, with fixed very small amplitude $\Omega_1 = 0.5$ and the initial phase between components given by $\phi = \pi/8$. The frequency ω of the time-perturbed Raman is varied within the region where resonant interferences are verified. For $\omega = 32$, the unperturbed case is also shown by a dashed line. As in Fig. 13, the nonlinear parameters are $\gamma = 1$ and $\beta = 0.5$. All quantities are in dimensionless units.

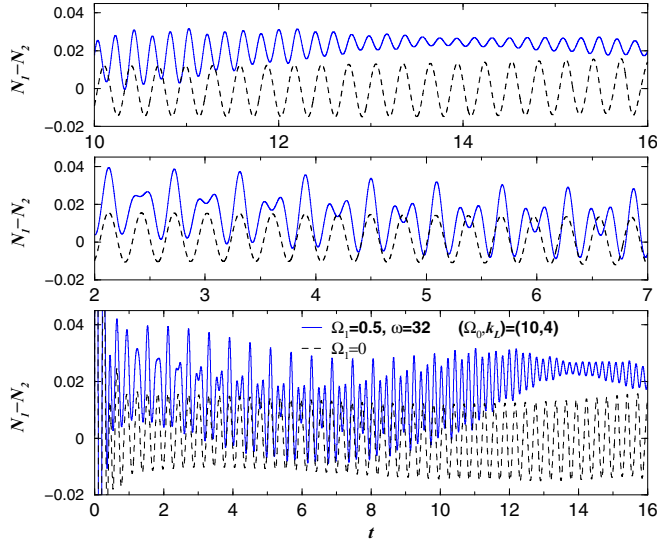


FIG. 15. The case with $\omega = 32$ (solid lines) was selected from Fig. 14, including the unperturbed case (black dashed line). In the lower panel, we have a larger-time interval ($0 \leq t \leq 16$), with the middle and upper panels having smaller intervals given by $2 \leq t \leq 7$ and $10 \leq t \leq 16$, respectively. All quantities are dimensionless.

perturbation are verified only in the interval $39 > \omega > 22$, with maxima interferences occurring for $\omega \sim 32$ (the middle panel, where we have also included with a dashed line the unperturbed case for comparison). The results for $\omega > 39$ and < 22 are almost identical to the nonperturbed case, $\Omega_1 = 0$. Therefore, we select the case with $\omega = 32$ to show in more detail the oscillating behavior, which is presented in Figs. 15 and 16. In the lower panel of Fig. 15, we consider a larger-time interval with $0 \leq t \leq 16$ (lower panel). The middle panel ($2 \leq t \leq 7$) serves to show the change in the frequency of the oscillations, such that for each two cycles another cycle is emerging, which

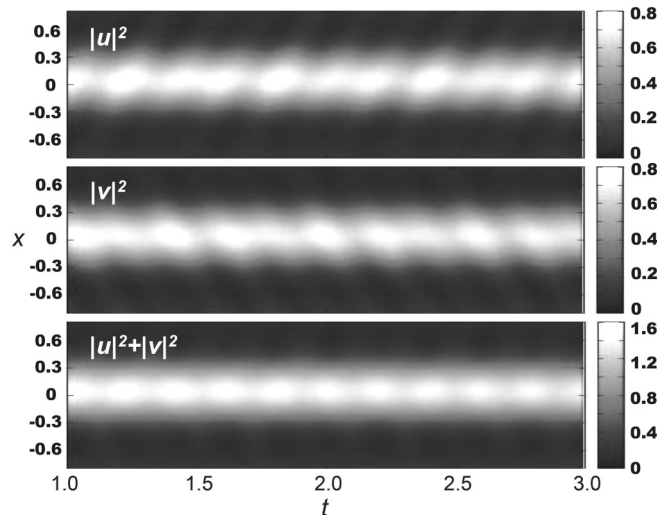


FIG. 16. Density plots $|u(x,t)|^2$, $|v(x,t)|^2$, and $|u(x,t)|^2 + |v(x,t)|^2$, corresponding to the case shown in the lower set of three panels of Fig. 15, at positions x for the time interval $1 < t < 3$. All quantities are in dimensionless units.

can be verified for $10 \leq t \leq 16$. In all three given panels, for comparison we include, by a dashed line, the unperturbed case.

IV. HIGH-FREQUENCY MODULATIONS AND AVERAGED GP EQUATIONS

In the case in which we have rapidly and strongly varying Raman oscillations $\Omega(t)$, it is useful to derive the corresponding averaged GP equation such that one can reduce the time-dependent modulated Raman frequency to the constant one Ω_0 by renormalizing the spin-orbit coupling and the nonlinear parameters, as we show in this section. By matching the averaged results with the full-numerical ones, obtained with real-time evolution, we also verify numerically how fast and strong the time oscillations should be in order to validate the averaging approach. In order to derive the average over a rapid modulations system of equations, we first apply the following unitary transformation [15,21] in Eq. (1):

$$\Phi \equiv \begin{pmatrix} U \\ V \end{pmatrix} = \begin{pmatrix} \cos(q) & i \sin(q) \\ i \sin(q) & \cos(q) \end{pmatrix} \begin{pmatrix} u \\ v \end{pmatrix}, \quad (16)$$

where $q \equiv q(t) = (\Omega_1/\omega) \sin(\omega t)$ is given by the requirement that the time-dependent part of the Raman frequency does not appear explicitly in the coupled equation for Φ . When performing the time averaging of the interactions together with the SOC parameter k_L , the parameters of the nonlinear interaction also have to be renormalized. They are replaced by parameters that contain the zero-order Bessel function, considering that

$$\frac{1}{2\pi} \int_0^{2\pi} d(\omega t) \exp\left[\frac{in\Omega_1}{\omega} \sin(\omega t)\right] = J_0\left(\frac{n\Omega_1}{\omega}\right). \quad (17)$$

Then, by defining $\chi \equiv 2\Omega_1/\omega$, the coupled equation, averaged over the period of rapid modulations, with $V_{tr} = 0$, can be written as [15]

$$i \frac{\partial \Phi}{\partial t} = \left[-\frac{1}{2} \frac{\partial^2}{\partial x^2} - ik_L J_0(\chi) \sigma_z \frac{\partial}{\partial x} + \Omega_0 \sigma_x \right] \begin{pmatrix} U \\ V \end{pmatrix} - \begin{pmatrix} \alpha_+ |U|^2 + \alpha_1 |V|^2 & \alpha_0 U^* V \\ \alpha_0 V^* U & \alpha_- |V|^2 + \alpha_1 |U|^2 \end{pmatrix} \begin{pmatrix} U \\ V \end{pmatrix}, \quad (18)$$

where

$$\begin{aligned} \alpha_0 &\equiv \left(\beta - \frac{1+\gamma}{2} \right) \frac{1 - J_0(2\chi)}{4}, \\ \alpha_{\pm} &\equiv \alpha_0 + \frac{1+\gamma}{2} \pm \frac{1-\gamma}{2} J_0(\chi), \\ \alpha_1 &\equiv \beta - 2\alpha_0. \end{aligned} \quad (19)$$

In the case of gauge symmetry, with $\beta = \gamma = 1$, we have $\alpha_0 = 0$ and $\alpha_{i \neq 0} = 1$, i.e., the nonlinear part of the above coupling equation for (U, V) is exactly the same as the ones obtained for (u, v) , such that the time averaging is only renormalizing the SOC parameter k_L to

$$\kappa_{\text{eff}} = k_L J_0\left(\frac{2\Omega_1}{\omega}\right), \quad (20)$$

as one can verify by comparing the coupled Eqs. (18) with (2). This approach for tuning of the SOC parameter has been

confirmed recently in an experiment reported in Ref. [17]. Therefore, when considering rapid variations of the Raman frequency, the spin-orbit coupling k_L can be tuned in order to control the solitons in a BEC with SOC. In particular, it can be quite useful to transform striped solitons to regular solitons, and vice versa. With the appropriate ratio between amplitude Ω_1 and frequency ω of the Raman oscillations, a given value of k_L for region II, where $k_L^2 > \Omega_0$, can be changed to $\kappa_{\text{eff}}^2 < \Omega_0$, where we obtain regular soliton solutions, such that all the theory developed before (in Secs. II and III) for the constant Raman frequency can be applied.

The above can be exemplified by the results shown in Fig. 3, which are for regular soliton solutions, with $k_L = 4$ and $\Omega_0 = 80$ and 20, respectively. These results are for region I, but can also be applied to the case in which we originally have k_L larger than Ω_0 , if the time modulation of the Raman frequency $\Omega(t)$, given by Eq. (5), is such that the ratio between Ω_1 and ω will give us $\kappa_{\text{eff}} = k_L J_0(\chi) = 4$. We could initially take $k_L = 10$, for example, as it is larger than Ω_0 in both of the cases shown in Fig. 3, with the parameters of the time-modulating Raman such that $J_0(\chi) = 0.4$.

When considering other values for the nonlinear parameters, as a general remark we noticed that stable soliton solutions are obtained for attractive two-body interactions. Another remark, when considering the averaged approach, is that for $\beta \neq 1$, we can also have conditions with zero in the off-diagonal terms of the nonlinear two-body matrix, which brings Eq. (18) to the same format as Eq. (2). This happens for $\beta = (1 + \gamma)/2$, with $\alpha_0 = 0$, $\alpha_1 = \beta$, and $\alpha_{\pm} = \beta \pm (1 - \beta)J_0(\chi)$. For the more general cases, as for $\alpha_0 \neq 0$ or $2\beta \neq (1 + \gamma)$, new terms appear that correspond to the effective four-wave mixing ($\sim U^2 V^*$, $V^2 U^*$). These terms can lead to new possibilities, such as a way to control the atom-number oscillations between two components (internal Josephson effect [35,36]).

A. The solitonic solutions

The solitonic solutions for the averaged GP equations can be found by applying the multiscale method [11] to the two regions defined by the linear spectrum, which are given by Eq. (3). By using this multiscale method for values of the chemical potential near the bottom of the dispersive curve, with $\mu = -\Omega_0 - \varepsilon^2 w_0$ ($\varepsilon \ll 1$), where ω_0 is the free parameter, in region I (see Fig. 1), we obtain

$$u_s^{(I)} = \varepsilon \sqrt{\frac{2w_0}{\alpha_+ + \alpha_1 + \alpha_0}} \operatorname{sech}\left(\varepsilon \sqrt{\frac{2w_0}{\Delta_{\text{eff}}}} x\right), \quad (21)$$

$$v_s^{(I)} = -u_s^{(I)}, \quad \Delta_{\text{eff}} = 1 - \frac{\kappa_{\text{eff}}^2}{\Omega_0}. \quad (22)$$

In region II, where $\kappa_{\text{eff}}^2 > \Omega_0$ and two minima exist in the momentum space, we can take the chemical potential as $\mu = w_{\text{min}} - \varepsilon^2 w_0$ (see Fig. 1), with

$$w_{\text{min}} = \frac{1}{2}\kappa_0^2 - \kappa_{\text{eff}}^2, \quad \kappa_0 \equiv \pm \sqrt{\kappa_{\text{eff}}^2 - \Omega_0/\kappa_{\text{eff}}^2}, \quad (23)$$

and look for solutions of the form $(u, v) = \varepsilon(A, B) \exp(\pm i\kappa_0 x)$. For the result, we obtain a bright-soliton solution with the form

given by

$$\begin{pmatrix} u_s^{(II)} \\ v_s^{(II)} \end{pmatrix} = \begin{pmatrix} \Omega_0 \\ -\kappa_{\text{eff}}(\kappa_{\text{eff}} \pm \kappa_0) \end{pmatrix} \frac{\varepsilon f(x) e^{\pm i\kappa_0 x - i\mu t}}{\sqrt{|\kappa_{\text{eff}} \pm \kappa_0|}}, \quad (24)$$

where

$$f(x) = \frac{\sqrt{2w_0\kappa_{\text{eff}}}}{\sqrt{\alpha_+(\kappa_{\text{eff}}^4 + \kappa_{\text{eff}}^2\kappa_0^2) + (\alpha_1 + \alpha_0)\Omega_0^2}} \times \operatorname{sech}\left(\varepsilon \sqrt{\frac{2w_0\kappa_{\text{eff}}^2}{\kappa_0^2}} x\right). \quad (25)$$

Analogically, the striped soliton solution can be found as linear superpositions of solutions represented by Eq. (24). As already known, these solutions are used to describe the longitudinal and transversal spin polarizations of the solitons [11], with

$$\begin{aligned} \langle \sigma_z \rangle &= \frac{1}{N} \int_{-\infty}^{\infty} dx (|u|^2 - |v|^2), \\ \langle \sigma_x \rangle &= \frac{1}{N} \int_{-\infty}^{\infty} dx (u^* v + uv^*), \\ N &\equiv \int_{-\infty}^{\infty} dx (|u|^2 + |v|^2). \end{aligned} \quad (26)$$

In region I, where $\Omega_0 < \kappa_{\text{eff}}^2$, the solitons are fully polarized along the x axis. The same approach is valid for striped solitons in region II. However, the polarization along z is not zero for solitons with momentum $k = \pm\kappa_0$. From Eqs. (21)–(25), we obtain

$$\langle \sigma_z \rangle^{(II)} = -\sqrt{1 - \Omega_0^2/\kappa_{\text{eff}}^4}, \quad \langle \sigma_x \rangle^{(II)} = -\frac{\Omega_0}{\kappa_{\text{eff}}^2}. \quad (27)$$

Thus, by varying the ratio χ , and so κ_{eff} , we can observe quantum phase transition in the pseudospin polarization $\langle \sigma_z \rangle^{(II)}$ of the soliton. These results for the soliton polarization are analogous to the ones obtained for the repulsive BEC in the framework of the Dicke model in [15].

With the understanding that the results obtained in this section are valid in a more general context for constant values of the Raman frequency, with Fig. 17 we show the dependence of the energy and chemical potential on the number of atoms N for the case in which $\Omega_0 = 0$, $\beta = \gamma = 1$, $k_L = 8$, when considering $\chi = 2\Omega_1/\omega = 3.7152$ (with both Ω_1 and ω very large), which give us $J_0(\chi) = -0.4$. Note that in this simple case, we have, for the dispersion relation (3), $w_{\pm}(k) = k(k/2 \pm k_L)$, with the signal of the give SOC moving from the original $k_L = 8$ to a negative one, $\kappa_{\text{eff}} = -3.2$. Therefore, after considering the time averaging, in this particular case with $\Omega_0 = 0$, we obtain $w_{\pm}(k) = k(k/2 \pm \kappa_{\text{eff}})$ such that both w_+ and w_- have the same shape as w_- shown in Fig. 1, but with minima given at $k = -\kappa_0$ (for w_+), and $k = \kappa_0$ (for w_-). As we are in region II, even after the averaging, the soliton solutions are not regular ones and are expected to have shapes with some oscillations. In Fig. 18, we illustrate the kind of solutions we obtain by presenting the real and imaginary parts of the wave-function components when considering the particular case with $N = 6.86$, $E = -48.6$, and $\mu = -11$.

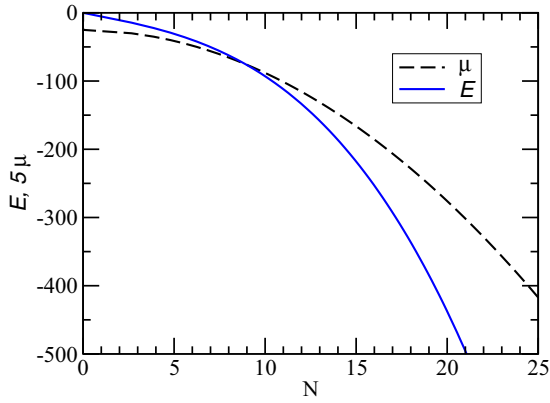


FIG. 17. The energy E (solid line) and chemical potential μ (dashed line) are shown as functions of the atom number N by considering the parameter $\beta = \gamma = 1$, $k_L = 8$, $\Omega_0 = 0$, and $\chi = 2\Omega_1/\omega = 3.7152$ [$J_0(\chi) = -0.4$, $\kappa_{\text{eff}} = -3.2$], with $\varepsilon^2 w_0 = 0.4$. All quantities are in dimensionless units.

B. Full numerical versus averaged results

To conclude this section, we compare the time-evolution results obtained with the effective time-averaging approach (where the SOC parameter is κ_{eff}) with the ones obtained in real time, with the SOC parameter k_L and explicit Raman frequency modulated by $\Omega_1 \cos(\omega t)$.

With Figs. 19–21, we exemplify our results for the comparison of averaged results with real-time-dependent numerical simulations. All the results for the time-averaged formalism that are shown in these examples are verified to be numerically very stable in the time evolution.

The results given in Fig. 19 are for region I, with $\Omega_0 = 120$ ($> k_L^2$), by considering the SOC parameter $k_L = 8$. For the time-dependent Raman frequency, we assume Ω_1 and ω such that $\chi \sim 2.4$, implying that $J_0(\chi) = 0$. Therefore, in this case, the averaged SOC parameter is $\kappa_{\text{eff}} = 0$. As shown in the four panels, the averaged results present good agreement with the real-time simulations when Ω_1 is about 10 times or more larger than Ω_0 .

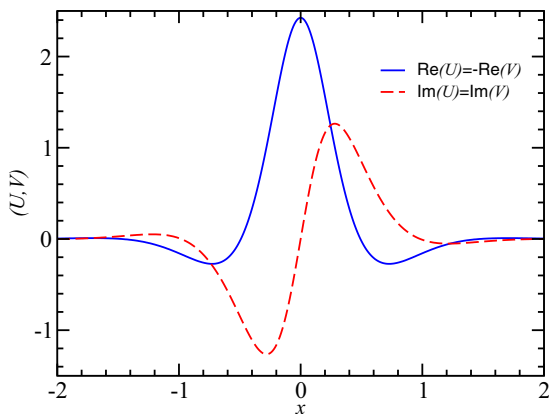


FIG. 18. The real (solid blue line) and imaginary (dashed red line) parts of the wave-function components are shown for $E = -48.6$, $N = 6.86$, $\mu = -11$, with the other parameters as in Fig. 17. All quantities are in dimensionless units.

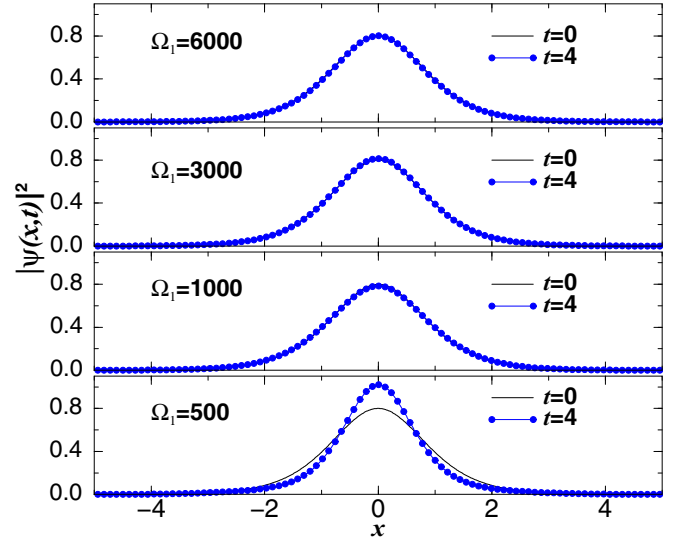


FIG. 19. Real-time evolution of the soliton profile for $\Omega_0 = 120$, $k_L = 8$, with $\beta = \gamma = 1$, considering several values of Ω_1 (shown inside the panels) and ω , such that $J_0(\chi) = 0$ ($\chi = 2.4$). At $t = 0$, the results in each of the panels coincide with the ones obtained with the averaged formalism (where $\kappa_{\text{eff}} = 0$). At larger times (represented by $t = 4$), we show that the agreement between real-time and averaged results is improved as one increases Ω_1 . The other parameters are $\beta = \gamma = 1$. All quantities are in dimensionless units.

For region II, we illustrate, with Figs. 20 and 21, two quite different combinations of Raman frequency and SOC parameters. In Fig. 20, we present our results obtained for $k_L = 8$ and $\Omega_0 = 12$, with Ω_1 and ω such that $\chi \sim 1.52$. As $J_0(\chi) = 1/2$ and $\kappa_{\text{eff}} = 4$, we are in region II ($\Omega_0 < \kappa_{\text{eff}}^2$). The results are shown for different values of $\Omega_1 = 50\chi = 76$ (lower panel),

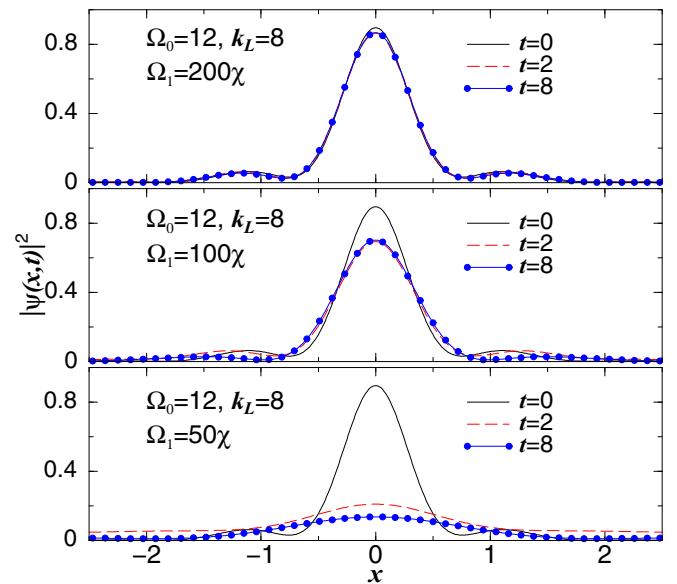


FIG. 20. Evolution of the soliton profile for $\Omega_0 = 12$, $k_L = 8$, with $\beta = \gamma = 1$, in three panels for different values of Ω_1 , with $\chi = 2\Omega_1/\omega = 1.52$ [such that $J_0(\chi) = 1/2$], implying that $\kappa_{\text{eff}} = 4$. In this case, we have $\kappa_0 = 2.65$. All quantities are in dimensionless units.

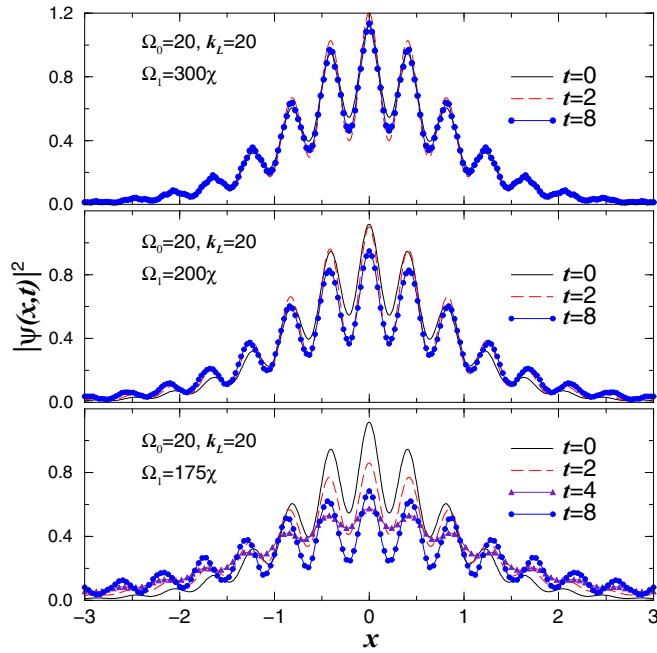


FIG. 21. The evolution of striped soliton profiles are shown in three panels, for $\Omega_0 = 20$ and $k_L = 20$, considering a few values of Ω_1 and ω in the real-time propagation. For $t = 0$, the results are the same ones obtained by the averaged formalism, where $\kappa_{\text{eff}} = -8$. In all the frames, the ratio between the parameters Ω_1 and ω is fixed, given by $\chi = 2\Omega_1/\omega = 3.7152$, implying $J_0(\chi) = -0.4$. In this case, we have $\kappa_0 = 7.60$. All quantities are in dimensionless units.

$= 100\chi = 152$ (middle panel), and $= 200\chi = 304$ (upper panel). The parameters used in this case correspond to one of the examples presented in Fig. 9 for Josephson oscillations, where we have constant $\Omega_0 = 12$, with $k_L = 4$. We should note that the striped solitons shown in Fig. 20 have the main maximum at the center, with only one pair of maxima visible on each side, due to the choice of parameters which are close to the border between the regions for striped and regular solitons.

In Fig. 21, we consider a case where the effective SOC becomes negative, and we are more deeply inside region II. Departing from a large value of $k_L = 20$, with the combinations of Ω_1 and ω , such that by fixing $\chi = 3.7152$ and $J_0(\chi) = -0.4$, we have $\kappa_{\text{eff}} = -8$. The results are shown in the three panels in Fig. 21. For comparison, in all three panels, we also present the averaged results, which are equal to the unperturbed case with $t = 0$. From our study of this case, we should also observe that for smaller values of Ω_1 , the real-time solutions become unstable, collapsing in a short-time interval. The real-time solutions shown in the lower panel, for $\Omega_1 = 175\chi$, already indicate this instability. When considering $\Omega_1 = 150\chi$, the solution was already collapsed even at $t = 2$.

By considering our results, exemplified in Figs. 19–21, as a general remark for the case of fast-time oscillations in the Raman frequency, our conclusion is that good agreements between the averaged results with the full-numerical simulations can be verified only for Ω_1 about 10 times larger than Ω_0 (where the frequency ω is of the order of Ω_1), which is an approximate minimal condition for the time modulations in the Raman frequency in order to keep the soliton solutions stable during time evolution.

In the next section, we summarize this work with our main conclusions.

V. CONCLUSIONS

In the present work, we have studied the existence and dynamics of solitons in Bose-Einstein condensates (BECs) with spin-orbit coupling (SOC) and attractive two-body interactions by considering two coupled atomic pseudospin components with general time-dependent Raman frequency, which can be constant, or slowly or rapidly modulated in time. For that, after defining the two possible regions where two different kinds of soliton solutions exist, i.e., regular or striped bright solitons, we first consider the Raman frequency varying slowly and linearly in time, such that we can study the transition between the two kinds of soliton solutions: from regular to striped ones, and vice versa. The regions are established by the relation between the SOC parameter k_L and the constant part of the Raman frequency, Ω_0 , such that we have regular solitons in region I, when $\Omega_0 > k_L^2$, and striped solitons in region II, for $\Omega_0 < k_L^2$. Next, we study the internal Josephson oscillations between the atom numbers in soliton components, which are controlled by a constant or periodically time-oscillating Raman parameter. Different parameter configurations are studied for SOC in BEC, with parametric resonances indicating a mechanism to control the soliton parameters, as well as the evolution of the solitons center of mass. As shown, we also present a variational analysis, valid particularly in the case that we obtain regular bright-soliton solutions. The full-numerical simulations have confirmed the corresponding predictions.

In the limit of high frequencies, the system is described by a time-averaged Gross-Pitaevskii formalism with renormalized nonlinear and SOC parameters and additional modified phase-dependent nonlinearities. Therefore, by comparing full-numerical simulations with averaged results, we have studied the lower limits for the frequency of the Raman oscillations in order to obtain stable soliton solutions. The results are shown in a few examples for both regions I and II. One should note that due to the normalization of the nonlinear interactions, new terms can emerge in the nonlinear coupling of the averaged system for BECs with tunable SOC, when compared with the original nonaveraged formalism. Corresponding to the *phase-dependent nonlinear coupling*, we have a term $\sim \alpha_0$ appearing in the off-diagonal matrix terms of the nonlinear coupling. This term can play an important role for nonstationary processes in BECs with SOC, as well as in the Josephson oscillations between components of solitons with nonzero phase differences. This matter requires further separate investigation.

The expected relevance of the present study is in the prediction of some effects as well as in the corresponding parameter control, in a possible BEC experiment, such as in ^7Li with attractive interatomic interactions, where the SOC can be engineered as an effective two-level atom by a uniform magnetic field B with two Raman laser beams. In this example, we have the linear transverse trap frequency, $\omega_{\perp}/(2\pi) = 1$ kHz, the number of atoms $N = 10^3$, and the wavelength of the Raman lasers given by $\lambda = 804$ nm. Therefore, the Raman frequency can vary in the interval $(0.1-10)E_L$, where $E_L = \hbar^2 k_L^2 / 2m$ is the recoil energy and $k_L = 2\pi/\lambda$. For $\Omega_0 = 0.1E_L/\hbar$, we obtain $\Omega_0 = 2\pi \times 30$ kHz. Then the frequency of modulations is as follows: for the resonant case, the dimensionless $\omega = 60$

corresponds to $\omega = 2\Omega_0 = 60$ kHz, and for the high-frequency limit, $\omega = 300$ corresponds to $\omega = 10\Omega_0 = 300$ kHz.

ACKNOWLEDGMENTS

The authors acknowledge partial support from Conselho Nacional de Desenvolvimento Científico e Tecnológico (re-

search grants [L.T. and A.G.] and Project No. 400716/2014-3 [F.K.A., M.B., and L.T.], Fundação de Amparo à Pesquisa do Estado de São Paulo (Projects No. 2017/05660-0 [L.T.] and No. 2016/17612-7 [A.G.]), and Coordenação de Aperfeiçoamento de Pessoal de Nível Superior (program PVS-CAPES/ITA [L.T.]). F.K.A. is also grateful to IFT-UNESP for providing local facilities.

-
- [1] H. Zhai, *Rep. Prog. Phys.* **78**, 026001 (2015).
- [2] T.-L. Ho and S. Zhang, *Phys. Rev. Lett.* **107**, 150403 (2011).
- [3] Y.-J. Lin, K. Jiménez-García, and I. B. Spielman, *Nature (London)* **471**, 83 (2011).
- [4] Y.-J. Lin, R. L. Compton, A. R. Perry, W. D. Phillips, J. V. Porto, and I. B. Spielman, *Phys. Rev. Lett.* **102**, 130401 (2009); Y.-J. Lin, R. L. Compton, K. Jiménez-García, J. V. Porto, and I. B. Spielman, *Nature (London)* **462**, 628 (2009).
- [5] J.-R. Li, J. Lee, W. Huang, S. Burchesky, B. Shteynas, F.Ç. Top, A. O. Jamison, and W. Ketterle, *Nature (London)* **543**, 91 (2017).
- [6] Y. A. Bychkov and E. I. Rashba, *J. Phys. C* **17**, 6039 (1984).
- [7] G. Dresselhaus, *Phys. Rev.* **100**, 580 (1955).
- [8] V. Galitskii and I. B. Spielman, *Nature (London)* **494**, 49 (2013).
- [9] M. Merkl, A. Jacob, F. E. Zimmer, P. Öhberg, and L. Santos, *Phys. Rev. Lett.* **104**, 073603 (2010).
- [10] Y. Xu, Y. Zhang, and B. Wu, *Phys. Rev. A* **87**, 013614 (2013).
- [11] V. Achilleos, D. J. Frantzeskakis, P. G. Kevrekidis, and D. E. Pelinovsky, *Phys. Rev. Lett.* **110**, 264101 (2013).
- [12] D. A. Zezyulin, R. Driben, V. V. Konotop, and B. A. Malomed, *Phys. Rev. A* **88**, 013607 (2013).
- [13] L. Salasnich and B. A. Malomed, *Phys. Rev. A* **87**, 063625 (2013).
- [14] Y. V. Kartashov, V. V. Konotop, and F. Kh. Abdullaev, *Phys. Rev. Lett.* **111**, 060402 (2013).
- [15] Y. Zhang, G. Chen, and C. Zhang, *Sci. Rep.* **3**, 1937 (2013); Y. Zhang, L. Mao, and C. Zhang, *Phys. Rev. Lett.* **108**, 035302 (2012).
- [16] M. Salerno, F. Kh. Abdullaev, A. Gammal, and L. Tomio, *Phys. Rev. A* **94**, 043602 (2016).
- [17] K. Jiménez-García, L. J. LeBlanc, R. A. Williams, M. C. Beeler, C. Qu, M. Gong, C. Zhang, and I. B. Spielman, *Phys. Rev. Lett.* **114**, 125301 (2015).
- [18] J. Struck *et al.*, *Science* **333**, 996 (2011).
- [19] F. Meinert, M. J. Mark, K. Lauber, A. J. Daley, and H.-C. Nägerl, *Phys. Rev. Lett.* **116**, 205301 (2016).
- [20] F. Kh. Abdullaev, P. G. Kevrekidis, and M. Salerno, *Phys. Rev. Lett.* **105**, 113901 (2010).
- [21] H. Susanto, P. G. Kevrekidis, F. Kh. Abdullaev, and B. A. Malomed, *J. Comput. Appl. Math.* **235**, 3883 (2011).
- [22] M. Albiez, R. Gati, J. Fölling, S. Hunsmann, M. Cristiani, and M. K. Oberthaler, *Phys. Rev. Lett.* **95**, 010402 (2005).
- [23] S. Levy, E. Lahoud, I. Shomroni, and J. Steinhauer, *Nature (London)* **449**, 579 (2007).
- [24] M. Abbarchi, A. Amo, V. G. Sala, D. D. Solnyshkov, H. Flayac, L. Ferrier, I. Sagnes, E. Galopin, A. Lemaître, G. Malpuech, and J. Bloch, *Nat. Phys.* **9**, 275 (2013).
- [25] P. Zou and F. Dalfovo, *J. Low Temp. Phys.* **177**, 240 (2014).
- [26] J. J. G. Ripoll and V. M. Pérez-García, *Phys. Rev. A* **59**, 2220 (1999); J. J. Garcia-Ripoll, V. M. Pérez-García, and P. Torres, *Phys. Rev. Lett.* **83**, 1715 (1999).
- [27] P. G. Kevrekidis, A. R. Bishop and K. O. Rasmussen, *J. Low Temp. Phys.* **120**, 205 (2000).
- [28] L. Salasnich, A. Parola, and L. Reatto, *J. Phys. B* **35**, 3205 (2002).
- [29] C. Tozzo, M. Krämer, and F. Dalfovo, *Phys. Rev. A* **72**, 023613 (2005).
- [30] W. Cairncross and A. Pelster, *Eur. Phys. J. D* **68**, 106 (2014).
- [31] F. Kh. Abdullaev, A. Gammal, and L. Tomio, *J. Phys. B* **49**, 025302 (2016).
- [32] S. Cao, C.-J. Shan, D.-W. Zhang, X. Qin, and J. Xu, *J. Opt. Soc. Am. B* **32**, 201 (2015).
- [33] M. Britka, A. Gammal, and L. Tomio, *Phys. Lett. A* **359**, 339 (2006).
- [34] L. Wen, Q. Sun, Y. Chen, D.-S. Wang, J. Hu, H. Chen, W.-M. Liu, G. Juzeliūnas, B. A. Malomed, and A.-C. Ji, *Phys. Rev. A* **94**, 061602(R) (2016).
- [35] D.-W. Zhang, L.-B. Fu, Z. D. Wang, and S.-L. Zhu, *Phys. Rev. A* **85**, 043609 (2012); Y. Cheng, G. Tang, and S. K. Adhikari, *ibid.* **89**, 063602 (2014); C. Paré and M. Florjańczyk, *ibid.* **41**, 6287 (1990); Y. V. Kartashov, V. V. Konotop, and D. A. Zezyulin, *ibid.* **90**, 063621 (2014).
- [36] A. Smerzi, S. Fantoni, S. Giovanazzi, and S. R. Shenoy, *Phys. Rev. Lett.* **79**, 4950 (1997); S. Raghavan, A. Smerzi, S. Fantoni, and S. R. Shenoy, *Phys. Rev. A* **59**, 620 (1999).
- [37] F. Kh. Abdullaev and R. A. Kraenkel, *Phys. Rev. A* **62**, 023613 (2000); *Phys. Lett. A* **272**, 395 (2000).
- [38] G. L. Salmond, C. A. Holmes, and G. J. Milburn, *Phys. Rev. A* **65**, 033623 (2002).
- [39] E. Boukobza, M. G. Moore, D. Cohen, and A. Vardi, *Phys. Rev. Lett.* **104**, 240402 (2010).
- [40] L. D. Landau and E. M. Lifshitz, *Mechanics* (Pergamon Press, Oxford, 1973).
- [41] J. Hou, X.-W. Luo, K. Sun, T. Bersano, V. Gokhroo, S. Mossman, P. Engels, and C. Zhang, *Phys. Rev. Lett.* **120**, 120401 (2018).